Delft University of Technology

A highly selective and stable ZnO-ZrO$_2$ solid solution catalyst for CO$_2$ hydrogenation to methanol

Wang, Jijie; Li, Guanna; Li, Zelong; Tang, Chizhou; Feng, Zhaochi; An, Hongyu; Liu, Hailong; Liu, Taifeng; Li, Can

Important note
To cite this publication, please use the final published version (if applicable).
Please check the document version above.

CHEMISTRY

A highly selective and stable ZnO-ZrO₂ solid solution catalyst for CO₂ hydrogenation to methanol

Jijie Wang,[1]* Guanna Li,[1,2]* Zelong Li,[1] Chizhou Tang,[1] Zhaochi Feng,[1] Hongyu An,[1] Hailong Liu,[1] Taifeng Liu,[1] Can Li[1]†

Although methanol synthesis via CO hydrogenation has been industrialized, CO_2 hydrogenation to methanol still confronts great obstacles of low methanol selectivity and poor stability, particularly for supported metal catalysts under industrial conditions. We report a binary metal oxide, ZnO-ZrO₂ solid solution catalyst, which can achieve methanol selectivity of up to 86 to 91% with CO_2 single-pass conversion of more than 10% under reaction conditions of 5.0 MPa, 24,000 ml/(g hour), H_2/CO_2 = 3:1 to 4:1, 320° to 315°C. Experimental and theoretical results indicate that the synergetic effect between Zn and Zr sites results in the excellent performance. The ZnO-ZrO₂ solid solution catalyst shows high stability for at least 500 hours on stream and is also resistant to sintering at higher temperatures. Moreover, no deactivation is observed in the presence of 50 ppm SO_2 or H_2S in the reaction stream.

INTRODUCTION

Global environmental changes caused by huge amounts of anthropogenic CO_2 emissions have become a worldwide concern. However, CO_2 is an abundant and sustainable carbon resource. It is highly desired to develop technologies to convert CO_2 into valuable chemicals. Among the strategies considered, catalytic hydrogenation of CO_2 to methanol using the hydrogen from renewable energy sources has received much attention, because methanol not only is an excellent fuel but also can be transformed to olefins and other high value-added chemicals commonly obtained from fossil fuels (1).

Much progress has been made in the development of supported metal catalysts for CO_2 hydrogenation, such as Cu/ZnO/Al₂O₃ (2–10), Cu/ZrO₂ (2–5, 11–13), and Pd/ZnO (2–5, 14, 15). Among these, the Cu/ZnO/Al₂O₃ catalyst was the most efficient and has been extensively studied. However, one of the problems for these catalysts is the low methanol selectivity caused by reverse water–gas shift (RWGS) reaction. The even more severe problem is the rapid deactivation caused by produced water, which accelerates the sintering of Cu active component during the CO_2 hydrogenation (16). Although more efficient "georgeite" Cu-based catalyst (17), Cu(Au)/CeO$_x$/TiO₂ (18, 19), and Ni(Pd)-Ga (20–22) catalysts have been reported, the selectivity toward methanol is lower than 60% under their reported conditions. Recently, higher methanol selectivity is reported for In₂O₃ (23–25). However, this is compromised by low CO_2 conversion (25). Up to now, we are still lacking an efficient catalyst that enables a CO_2 hydrogenation conversion above 10% with high methanol selectivity and stability to fulfill the requirements of large-scale production under industrial operation conditions. Here, we report a ZnO-ZrO₂ solid solution catalyst, which shows methanol selectivity of 86 to 91% at a CO_2 conversion of more than 10% under the conditions of 5.0 MPa, 24,000 ml/(g hour), H_2/CO_2 = 3:1 to 4:1, 320° to 315°C, demonstrated with a fixed-bed reactor. The catalyst shows excellent stability for more than 500 hours on stream, and it is promising for the conversion of CO_2 to methanol in industry.

RESULTS AND DISCUSSION

A series of x% ZnO-ZrO₂ catalysts (x% represents molar percentage of Zn, metal base) were prepared by the coprecipitation method, and their catalytic performances were investigated as shown in Fig. 1. ZrO₂ shows very low activity in methanol synthesis. ZnO shows a little activity and low methanol selectivity (table S1). However, the performance of the ZnO-ZrO₂ catalyst varies greatly with the Zn/(Zn + Zr) molar ratio (Fig. 1A). The catalytic activity is significantly enhanced and reaches the maximum for CO_2 conversion when the Zn/(Zn + Zr) molar ratio is close to 13%. This is also where the methanol selectivity (mainly methanol and CO as the products) is approaching the maximum (fig. S1). Therefore, the highest space-time yield (STY) of methanol is achieved for the ZnO-ZrO₂ catalyst at the Zn/(Zn + Zr) molar ratio of 13%, and hereafter, it represents the optimized catalyst. It is worth noting that the CO_2 conversion of 13% ZnO-ZrO₂ is about 1.3 and 14 times of those for ZnO and ZrO₂, respectively, and the methanol selectivity is increased from no more than 30% for ZnO or ZrO₂ to more than 80% for 13% ZnO-ZrO₂. More interestingly, the activity of 13% ZnO-ZrO₂ is about six times of that for mechanically mixed ZnO and ZrO₂ in the same composition as 13% ZnO-ZrO₂ (inset in Fig. 1A), indicating that there is a strong synergetic effect between these two components in the catalytic activity of CO_2 hydrogenation.

Figure 1B shows that when increasing the reaction temperature, the selectivity of methanol decreases, whereas the conversion of CO_2 increases. When the conversion reaches 10% at 320°C, the selectivity of methanol can still be kept at 86%. Higher pressure, gas hourly space velocity (GHSV), and H_2/CO_2 ratio are beneficial to the methanol selectivity (fig. S2). Methanol selectivity can be as high as 91% when H_2/CO_2 is increased to 4:1 with a CO_2 conversion of 10% at 315°C.

Figure 1C shows that there is no deactivation of the 13% ZnO-ZrO₂ catalyst in CO_2 hydrogenation, and no deterioration in methanol selectivity for more than 500 hours on stream at least. Stability is a fatal issue for methanol synthesis from either CO or CO_2 hydrogenation on most supported metal catalysts because most methanol synthesis catalysts are easily deactivated at higher temperatures due to the sintering effect. To further test the thermal stability of the catalyst, the reaction temperature was elevated from 320° to 400°C, kept for 24 hours, and then cooled down to 320°C. No deactivation is observed after this annealing treatment. To our surprise, this catalyst also shows the resistance to sulfur-containing molecules in the stream with 50 parts per million (ppm) SO_2
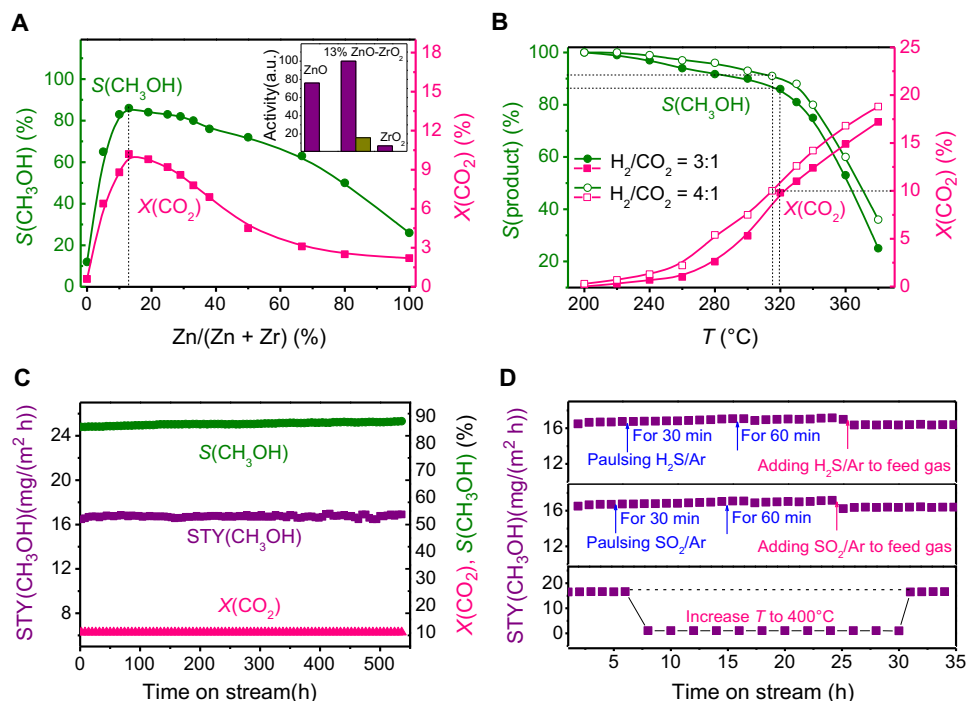
Fig. 1. Catalytic performance of the ZnO-ZrO₂ catalyst. (A) Dependence of catalytic performance at 320°C on the Zn/(Zn + Zr) molar ratio. Inset: purple, normalized activities for ZnO, 13% ZnO-ZrO₂, and ZrO₂ by specific surface area; dark yellow, normalized activities for mechanically mixed ZnO and ZrO₂ in the same composition. (B) Catalytic performance at the reaction temperatures from 200° to 380°C with H₂/CO₂ = 3:1 and 4:1. (C) Catalyst stability test in 550 hours. (D) Catalyst stability toward the S-containing molecules (50 ppm H₂S or SO₂ in Ar) and annealing. In S experiments, there are two gas paths: one is 50 ppm H₂S(SO₂)/Ar and the other is CO₂/H₂/Ar. Pulsing experiment was carried out by turning on the S gas for 30 min and 60 min and then turning off after the CO₂ + H₂ reaction reached its steady state. After several pulses, the two gas paths were turned on simultaneously. Standard reaction conditions: 5.0 MPa, H₂/CO₂ = 3:1, 320°C, GHSV = 24,000 ml/(g hour), using a tubular fixed-bed reactor with the 13% ZnO-ZrO₂ catalyst.

or H_2S (Fig. 1D). The sulfur-containing molecules are always present in CO_2 sources from flue gas produced from coal or biomass burning. Therefore, the high stability of the catalyst toward the sulfur-containing molecules makes the catalyst viable in industrial processes and superior to supported metal catalysts.

X-ray diffraction (XRD) patterns show that the ZrO_2 prepared by the coprecipitation method is mainly in the monoclinic phase mixed with some in the tetragonal phase (Fig. 2A and fig. S3). Adding ZnO (5 to 33%) to ZrO_2 leads to the phase change of ZrO_2 from monoclinic to tetragonal or cubic (not distinguishable from tetragonal). The phase of ZnO was detected for samples with ZnO concentrations of up to 50%, indicating that the $ZnO-ZrO_2$ solid solution might be formed with ZnO contents in the range below 50%. The interplanar spacing of 13% $ZnO-ZrO_2$, which is ca. 0.29 nm (Fig. 2B and fig. S4), is attributed to the tetragonal ZrO_2 (011). However, element distribution analysis shows that Zn is highly dispersed in ZrO_2 (Fig. 2C). Considering that the ionic radius of Zn^{2+} (0.74 Å) is smaller than that of Zr^{4+} (0.82 Å) (26), the interplanar spacing would be decreased when Zn^{2+} is incorporated into the lattice of ZrO_2. This is confirmed with the XRD results that the (011) spacing of ZrO_2 narrows, and the XRD from the (011) spacing of ZrO_2 shifts to a higher angle when the Zn concentration is increased from 5 to 33%. These facts further affirm the conclusion that $ZnO-ZrO_2$ is in a solid solution state, with Zn incorporated into the ZrO_2 lattice matrix (27).

Raman spectroscopy was used to further characterize the phase structure of the $ZnO-ZrO_2$ solid solution catalyst. Raman spectroscopy with different laser sources could detect phases in different depths due

to light absorption and light scattering $\{I \propto (1/\lambda)^4\}$. $ZnO-ZrO_2$ exhibits a strong ultraviolet-visible (UV-vis) absorption band at 215 nm (fig. S5A), so the shorter wavelength laser detects the phase in a relatively shallow layer. Therefore, the Raman spectroscopy with laser sources at 244, 266, and 325 nm could gradually detect phases from the skin layer to the bulk of the catalyst (fig. S5B) (28, 29). The phase near the utmost skin layer (the depth of skin layer is approximately 2 nm) is sensitively detected by UV Raman spectroscopy with a 244-nm excitation laser, as shown in Fig. 2D. The appearance of Raman peaks at 305, 342, and 378 cm⁻¹ indicates that the skin layer of pure ZrO_2 is in monoclinic. For 5 to 13% $ZnO-ZrO_2$ samples, when increasing the ZnO content from 5 to 13%, the spectrum evolved slightly from that of the monoclinic phase to one with an additional peak at 269 cm⁻¹, although the peaks in the range of 300 to 500 cm⁻¹ are similar to those of ZrO_2. The weak peak at 269 cm⁻¹ is due to the characteristics of the tetragonal phase (30, 31). This suggests that the skin layer phase of 13% $ZnO-ZrO_2$ might be in the transition state between monoclinic and tetragonal phases. The Raman spectrum with a 266-nm laser is dominated by peaks at 269 and 317 cm⁻¹ (Fig. 2D and fig. S5, C and D), which are due to the tetragonal phase of ZrO_2, and the Raman spectrum with a 325-nm laser gives a typical peak at 564 cm⁻¹ due to the cubic phase. These results suggest that underneath the skin layer of 13% $ZnO-ZrO_2$ is in the tetragonal phase, whereas the bulk is in the cubic phase. Note that the Raman signal of the monoclinic phase is much stronger than that of tetragonal and cubic phases. Therefore, the distorted phase in the surface region could be obscured by the monoclinic phase in Raman spectra. X-ray photoelectron spectroscopy (XPS) results show that the
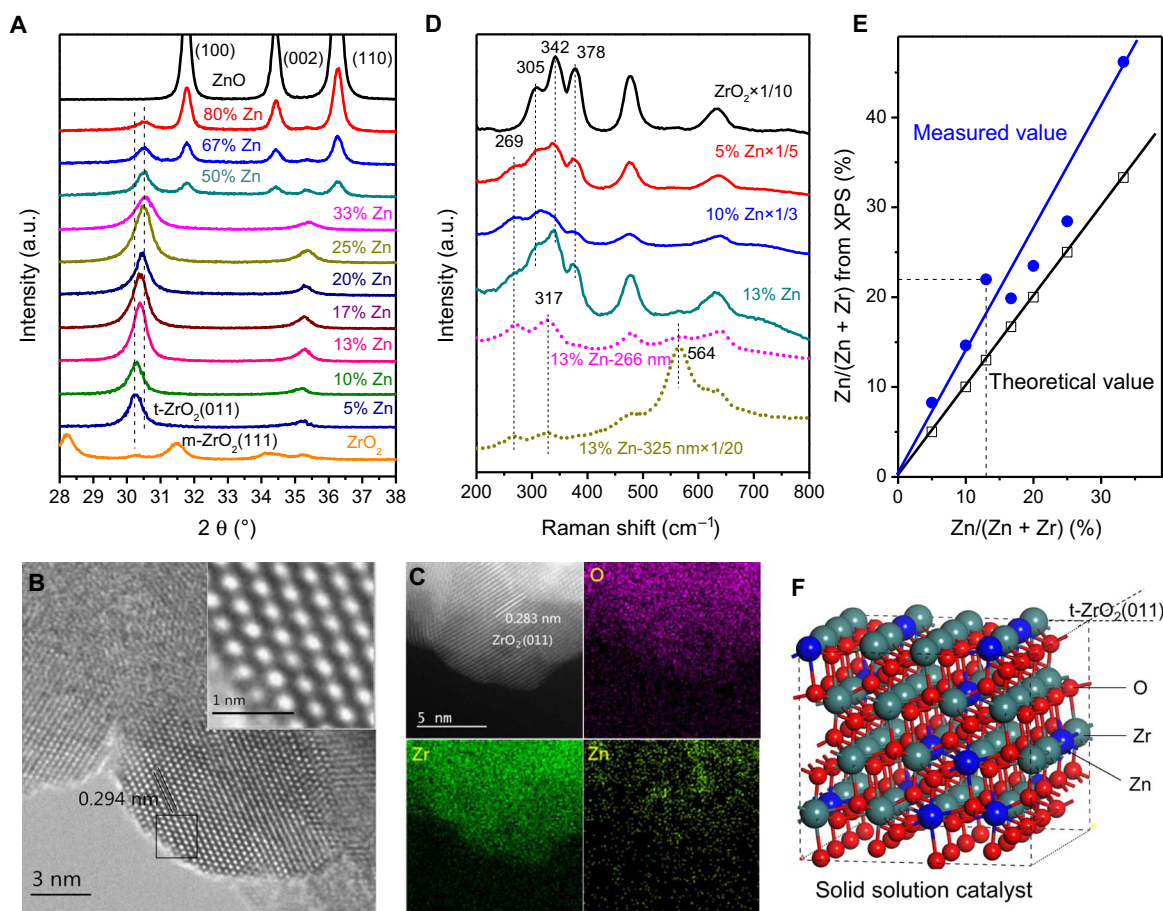
Fig. 2. Structural characterization of the ZnO-ZrO₂ catalyst. (**A**) XRD patterns of ZnO-ZrO₂. (**B**) High-resolution transmission electron microscopy (HRTEM) and (**C**) aberration-corrected scanning TEM–high-angle annular dark-field images and element distribution of 13% ZnO-ZrO₂. (**D**) Raman spectra of ZnO-ZrO₂ with 244-nm laser (solid line), 266-nm laser (pink dot line), and 325-nm laser (dark yellow dot line). (**E**) Zn concentration in the surface region of ZnO-ZrO₂ measured by XPS. (**F**) Schematic description of the ZnO-ZrO₂ solid solution catalyst model.

Zn concentration in the surface region is higher than the theoretical value (Fig. 2E), suggesting that Zn is relatively rich there. These facts indicate that the 13% ZnO-ZrO₂ catalyst is an imperfect solid solution in phase transition from skin layer to bulk, as schematically depicted in Fig. 2F.

CO₂-TPD (temperature-programmed desorption of CO₂) of catalysts shows that there are two desorption peaks: low (<320°C) and high (>320°C) temperature (Fig. 3A). The total CO₂ adsorption amounts for ZrO₂, 13% ZnO-ZrO₂, and ZrO₂ are 100, 82, and 82 mmol/m², respectively. CO₂ absorption capability below the reaction temperature, 320°C, follows the order ZrO₂ (100) > 13% ZnO-ZrO₂ (91) >> ZnO (32) (inset in Fig. 3A). ZrO₂ adsorbs much more CO₂ than does ZnO below the reaction temperature. Furthermore, the surface component of 13% ZnO-ZrO₂ is about 78% Zr and 22% Zn obtained from XPS (Fig. 2E), and the amount of adsorbed CO₂ on ZnO-ZrO₂ is about the same as that estimated from the sum of the amounts of CO₂ adsorbed on the individual components based on that normalized by specific surface area (inset in Fig. 3A). Therefore, it could be deduced that, at low temperatures, most of the CO₂ adsorbed by 13% ZnO-ZrO₂ is on the Zr sites.

The rate of HD formation from the H₂-D₂ exchange reaction normalized by specific surface area is as follows: ZnO (100) > 13% ZnO-ZrO₂ (89) >> ZrO₂ (7) (Fig. 3B), indicating that ZnO has much higher

activity in the H₂-D₂ exchange reaction than ZrO₂. Surprisingly, the activity of 13% ZnO-ZrO₂ is also much greater than that of ZrO₂, although ZrO₂ comprises 78% of the catalyst's specific surface area. If the two components kept their own activity in the 13% ZnO-ZrO₂ catalyst, the sum of their activities would be about 27, far less than the experimental result, which is 89. This suggests that there is a strong synergetic effect in the H₂ activation between the two sites, Zn and Zr. XPS shows that the binding energy of Zn in 13% ZnO-ZrO₂ is evidently reduced compared to that of ZnO, whereas the binding energy of Zr in 13% ZnO-ZrO₂ remains intact (fig. S6). This indicates that the electronic property of the Zn site is modified by the neighboring Zr site. H₂-TPR (temperature-programmed reduction of H₂) also shows that 13% ZnO-ZrO₂ is more easily reduced than ZnO and ZrO₂ (fig. S7). Therefore, on the basis of the H₂-D₂ exchange reaction and catalytic CO₂ hydrogenation reaction results, we could conclude that it is the synergetic effect between the Zn and Zr sites in the ZnO-ZrO₂ solid solution catalyst that significantly promotes the activation of H₂ and CO₂ and consequently results in the excellent catalytic performance in CO₂ hydrogenation. This is also shown experimentally from the fact that the 13% ZnO-ZrO₂ solid solution catalyst exhibits much higher activity and methanol selectivity than does mechanically mixed ZnO + ZrO₂ (13:87) or the supported 13% ZnO/ZrO₂ catalyst in CO₂ hydrogenation (Fig. 1A, table S2, and fig. S8).
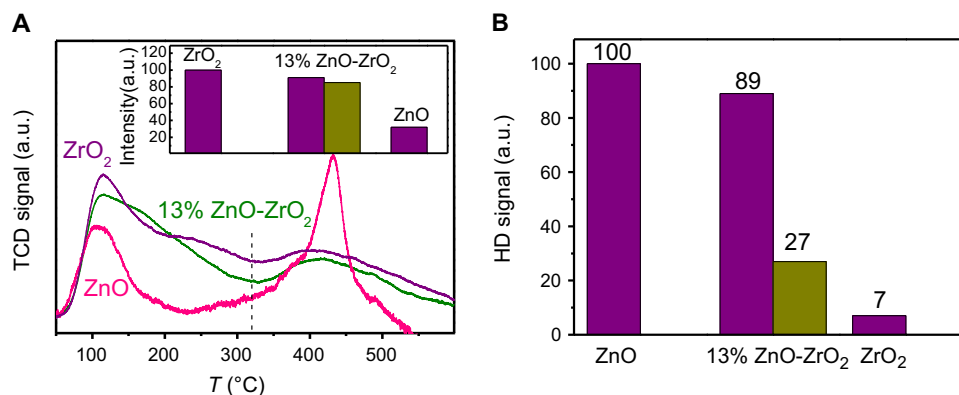
Fig. 3. CO$_2$ adsorption and H$_2$ activation. (**A**) CO$_2$-TPD on ZnO, ZrO$_2$, and 13% ZnO-ZrO$_2$ normalized by specific surface area. Inset: purple, normalized CO$_2$ adsorption below 320°C; dark yellow, normalized activities for mechanically mixed ZnO and ZrO$_2$ in the same composition as 13% ZnO-ZrO$_2$. (**B**) H$_2$-D$_2$ exchange reaction on ZnO, ZrO$_2$, and 13% ZnO-ZrO$_2$ at 280°C. Purple, normalized rate by specific surface area; dark yellow, normalized activities for mechanically mixed ZnO and ZrO$_2$ in the same composition as 13% ZnO-ZrO$_2$.

To understand the reaction mechanism on the solid solution catalyst, the surface species evolved in the reaction were monitored by in situ diffuse reflectance infrared Fourier transform spectroscopy (DRIFTS) (Fig. 4A). HCOO* and H$_3$CO* species were observed and identified (table S3) (*32–37*). The infrared (IR) peaks at 1595 and 1370 cm^{-1} are assigned to the asymmetric and symmetric OCO stretching vibrations, respectively, of adsorbed bidentate HCOO* species. The peaks at 2878 and 1382 cm^{-1} are assigned to the stretching vibration ν(CH) and bending vibration δ(CH), respectively. The peaks at 2931, 2824, and 1046 cm^{-1} are attributed to the H$_3$CO* species. The peaks at 2878 and 2824 cm^{-1} were used to follow the concentration changes of HCOO* and H$_3$CO* species. Figure 4B shows the varying tendency of the two species with time, and the products were detected by mass spectrometry (MS) (*38*). It can be seen that the surface HCOO* (based on IR peak intensity) reaches a steady state after a reaction for 30 min, whereas it takes 90 min for H$_3$CO* to reach its steady state. However, CH$_3$OH detected by MS reaches a steady state after 60 min. When CO$_2$ + H$_2$ was substituted for CO$_2$ + D$_2$, the amount of HCOO* and CH$_3$OH decreases (Fig. 4B and fig. S9), whereas the amount of DCOO* and CD$_3$OD increases. The DCOO* species appears and reaches a steady state after ca. 90 min; meanwhile, the total D-substituted products reach a steady state after ca. 90 min, as detected by MS. It is speculated that the HCOO* and CH$_3$O* species are likely intermediates of the CO$_2$ hydrogenation on the 13% ZnO-ZrO$_2$ solid solution catalyst. To verify the possible surface intermediate species, the IR spectra of surface species formed from CO$_2$ + H$_2$ were recorded as those in Fig. 4A, then the reaction gas phase of CO$_2$ + H$_2$ was switched to D$_2$, and the IR peaks at 2878 and 2824 cm^{-1} of the HCOO* and H$_3$CO* species, respectively, are declined rapidly and disappeared in 60 min (Fig. 4C). Correspondingly, two new peaks at 2165 and 2052 cm^{-1} due to the DCOO* and HD$_2$CO* species appeared first, grew somewhat, and then disappeared slowly. MS displays the HD$_2$COD product responding to the disappearance of the surface HCOO* and H$_3$CO* species at the same time (Fig. 4D). These evidences indicate that the surface HCOO* and H$_3$CO* species on the 13% ZnO-ZrO$_2$ solid solution catalyst can be hydrogenated to methanol.

Density functional theory (DFT) calculations were performed to understand the reaction mechanisms (details in the Supplementary Materials). Figure 5 shows the reaction diagram of CO$_2$ hydrogenation to methanol on the surface of ZnO-ZrO$_2$. Two major reaction pathways

were evaluated, that is, formate and CO pathways (*39, 40*). H$_2$ is adsorbed and dissociated on the Zn site. CO$_2$ is adsorbed on the coordination unsaturated Zr site (figs. S10 to S12). The formation of HCOO* species via CO$_2$* hydrogenation is energetically very favorable, which is coherent with the in situ DRIFTS observations. The terminal oxygen of H$_2$COO* (formed by HCOO* hydrogenation) can be protonated by an OH* group and forms a H$_2$COOH* species, of which the C-O bond is cleaved and thereby generates H$_2$CO* and OH* binding on Zr and Zn sites, respectively. The process of H$_2$COO* → H$_2$CO* + H$_2$O* is thermodynamically unfavorable ($\Delta_r G$ = 1.26 eV). The desorption energy of water from the surface is 0.60 eV. H$_2$CO* + H* → H$_3$CO* is an energetically favorable process ($\Delta_r G^{\ddagger}$ = −2.32 eV). H$_3$CO* species identified by theoretical calculation corresponds to the second most stable reaction intermediate detected by in situ DRIFTS. Finally, methanol is formed by H$_3$CO* protonation.

In principle, it is also possible to first produce CO* from CO$_2$* and then for CO* to undergo consecutive hydrogenation to form methanol. As shown in Fig. 5, OCOH* is much less stable than HCOO*. Furthermore, the reaction of CO$_2$* to OCOH* needs to overcome a barrier ($\Delta G^{\ddagger}$) of 0.69 eV, which is quite unfavorable compared to the barrier-less process of CO$_2$* + H* → HCOO*. Even if a fair amount of OCOH* can be present during the reaction, the weakly bonded CO* produced from OCOH* prefers to desorb from the surface rather than undergo hydrogenation reactions. Therefore, it is concluded that CO$_2$ hydrogenation to methanol on the surface of ZnO-ZrO$_2$ is through the formate pathway.

DFT calculations also suggest that the methanol selectivity of ZnO-ZrO$_2$ is higher than that of ZnO (*41, 42*). The formate pathway was evaluated on ZnO for CO$_2$ hydrogenation to methanol (figs. S13 to S16). The process of H$_2$COO* → H$_2$CO* + H$_2$O* is the most unfavorable step in thermodynamics. The energy barrier of this step is 1.37 eV, higher than that for ZnO-ZrO$_2$ (1.27 eV). Therefore, ZnO-ZrO$_2$ has a relatively higher methanol selectivity and a lower CO selectivity than ZnO. The results are consistent with the experimental results as well. The high methanol selectivity of ZnO-ZrO$_2$ solid solution is attributed to the synergetic effect in H$_2$ activation between the Zn and Zr sites, and the simultaneous activation of H$_2$ and CO$_2$ on the neighboring sites, Zn and Zr, respectively.

There has been an opinion that the CO$_2$ hydrogenation is similar to the CO hydrogenation, and the pathway of CO$_2$ to methanol is a CO
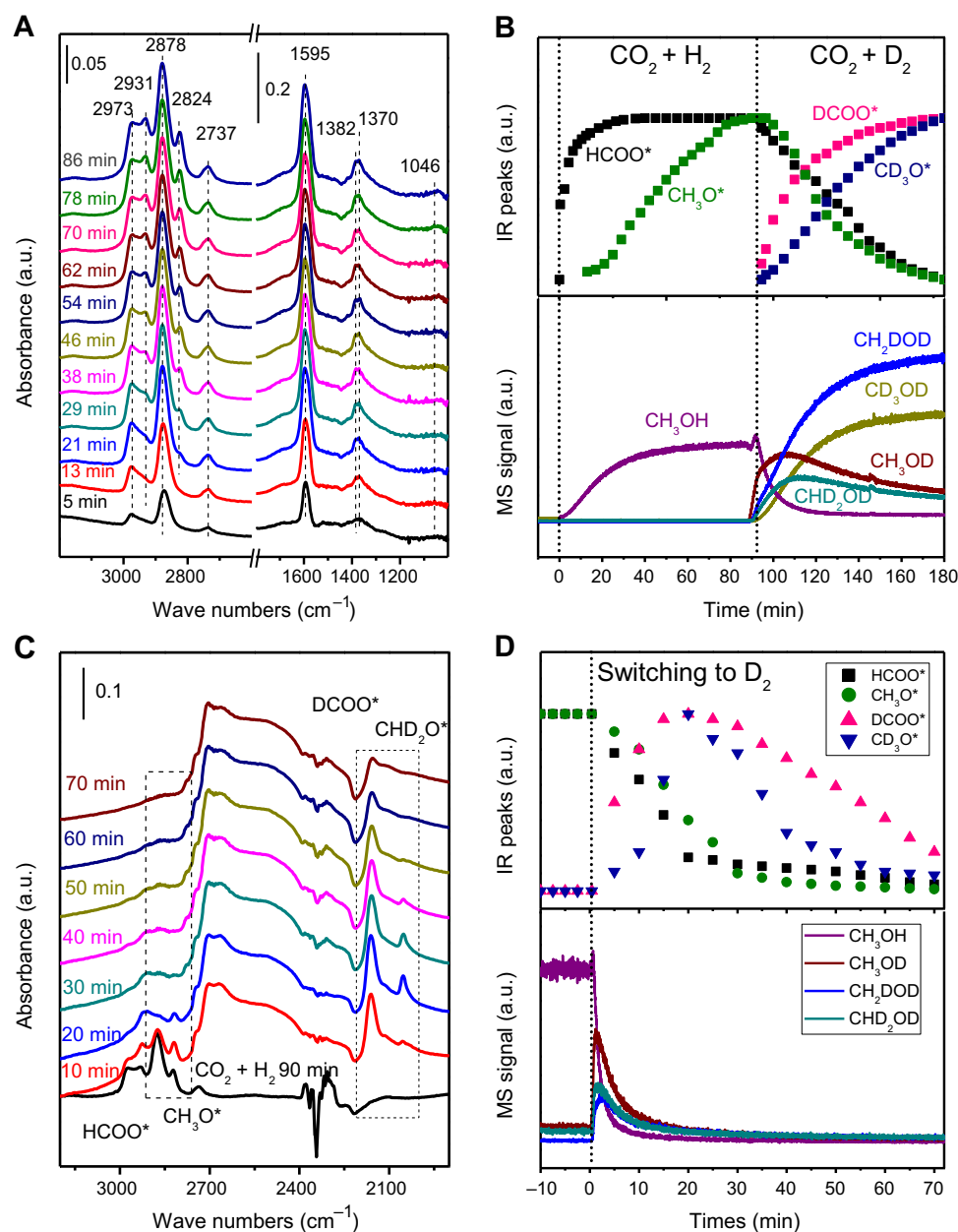
Fig. 4. Characterization of surface species. (**A**) In situ DRIFT spectra of surface species formed from the $CO_2 + H_2$ reaction. (**B**) DRIFT-MS of $CO_2 + H_2$ and $CO_2 + D_2$ reactions on 13% ZnO-ZrO$_2$. (**C**) In situ DRIFT spectra of surface species from $CO_2 + H_2$ and subsequently switched to D$_2$. (**D**) DRIFT-MS of $CO_2 + H_2$ and subsequently switched to D$_2$. Reaction conditions: 13% ZnO-ZrO$_2$ catalyst, 0.1 MPa, 280°C, 10 ml/min CO_2 + 30 ml/min H_2 (D_2).

pathway, where it is assumed that CO_2 hydrogenation to methanol is first to CO (by RWGS) and then the CO is hydrogenated to methanol (*13*, *18*). To clarify this issue, the 13% ZnO-ZrO$_2$ catalyst was also evaluated for CO + H$_2$ (fig. S17). Besides methanol as the major product, some additional products including dimethyl ether (DME) and methane were detected. The STY of methanol on the 13% ZnO-ZrO$_2$ catalyst from CO_2 hydrogenation is 2.5 times of that from CO hydrogenation at their optimized temperatures for methanol production. These facts indicate that the ZnO-ZrO$_2$ solid solution catalyst is especially active for CO_2 hydrogenation to methanol.

Whether formate species are involved in the methanol synthesis for Cu-based catalysts has been a controversial issue. For example, the latest

reports on Cu/ZrO$_2$ from Larmier *et al.* (*12*) and Kattel *et al.* (*13*) proposed very different mechanisms. According to the former, formate species was the reaction intermediate, whereas the latter stated that formate was a spectator. Very recently, Kattel *et al.* (*10*) proposed that the formate was an intermediate species for methanol on the Cu/ZnO catalyst. Because our ZnO-ZrO$_2$ catalyst is very different from the Cu-based one, the methanol formation mechanism might also be different. Our isotope labeling experiment and DFT calculation show that the formate species can be hydrogenated to methanol. However, at the moment, we still could not reach the conclusion that the formate species is the major active intermediate for methanol formation because it is difficult to determine how much of the observed formate species contributed to the methanol production.
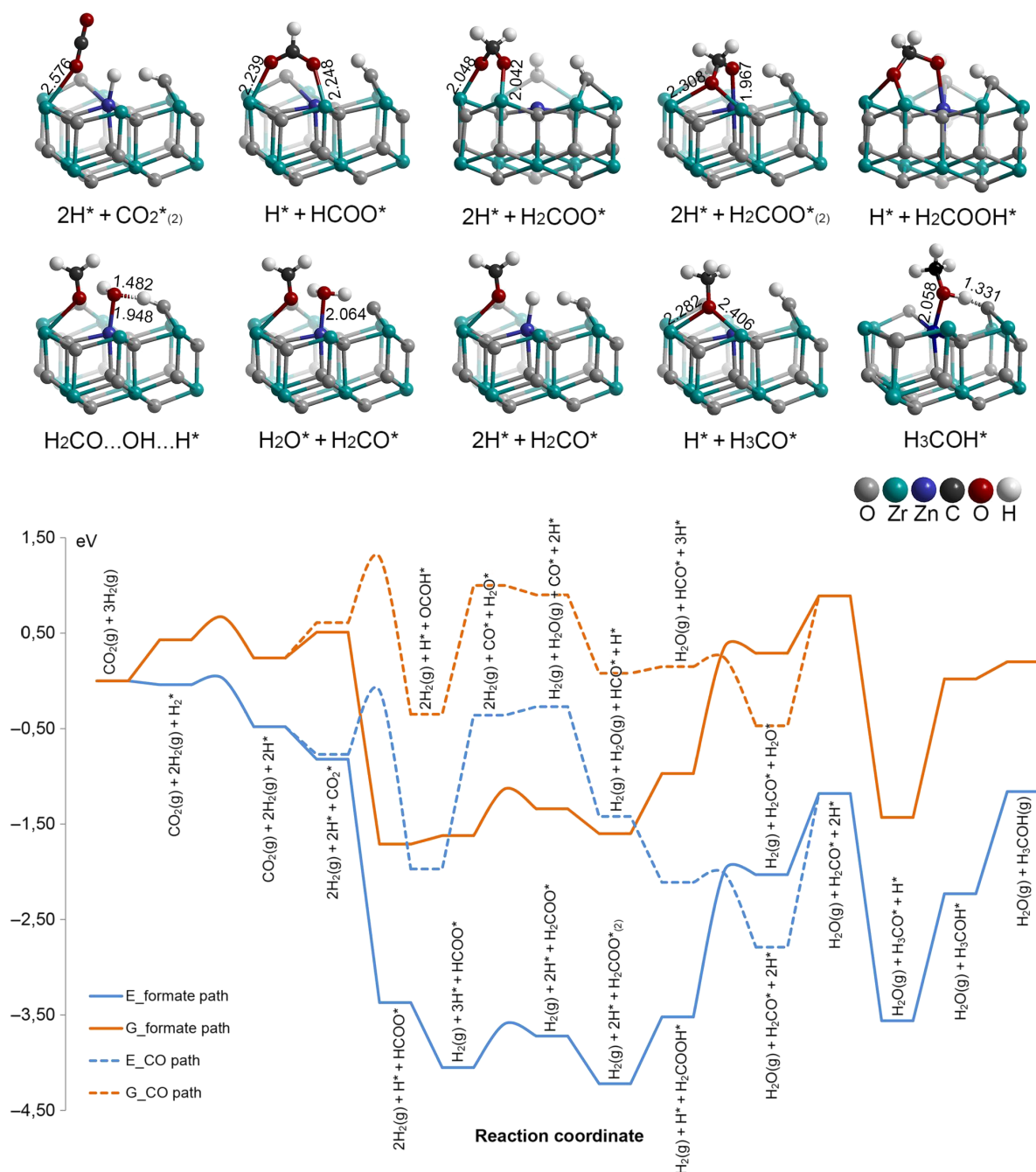
Fig. 5. DFT calculations. Reaction diagram [energy (E) and Gibbs free energy (G) at a typical reaction temperature of 593 K] of CO_2 hydrogenation to methanol on the (101) surface of the tetragonal $ZnO-ZrO_2$ model.

To compare the catalytic performance difference between the ZnO-ZrO_2 catalyst and Cu-based catalysts, a standard $Cu/ZnO/Al_2O_3$ catalyst was evaluated for CO_2 hydrogenation. The methanol selectivity varies from 82 to 5% at reaction temperatures from 200° to 320°C under identical conditions as those used for the 13% ZnO-ZrO_2 catalyst (fig. S18). The results are similar to those reported for the $Cu/ZnO/Al_2O_3$ catalyst in the literature (43, 44). It is seen that the selectivity of methanol on the Cu-based catalyst is lower than that on the 13% ZnO-ZrO_2 catalyst and markedly decreases when the reaction temperature was elevated. In addition, the stability of the $Cu/ZnO/Al_2O_3$ catalyst

was tested for sintering and sulfur poisoning (fig. S19). The activity of the catalyst shows a decrease of 25% for the reaction in 500 hours, and the activity drops even more quickly in the presence of 50 ppm SO_2; however, the 13% ZnO-ZrO_2 catalyst does not show any deactivation in 500 hours and SO_2 does not change the activity obviously either (Fig. 1, C and D). A controlled experiment demonstrated that the $Cu/ZnO/Al_2O_3$ catalyst was deactivated severely (at least 25% drop in activity) after a thermal treatment at 320°C, whereas the 13% ZnO-ZrO_2 catalyst does not show evident deactivation after a thermal treatment even at 400°C (Fig. 1D).

This work demonstrates that the binary metal oxide ZnO-ZrO$_2$ in the solid solution state is an active catalyst for converting CO$_2$ to methanol with high selectivity and stability. This solid solution catalyst opens a new avenue for CO$_2$ conversion by taking advantage of the synergetic effect between its multicomponents.

MATERIALS AND METHODS

Catalyst preparation

The 13% ZnO-ZrO$_2$ catalyst was taken as a typical example to describe the synthesis procedures: 0.6 g of Zn(NO$_3$)$_2$ · 6H$_2$O and 5.8 g of Zr(NO$_3$)$_4$ · 5H$_2$O were dissolved in a flask by 100 ml of deionized water. The precipitant of the 100-ml aqueous solution of 3.06 g of (NH$_4$)$_2$CO$_3$ was added to the aforementioned solution (at a flow rate of 3 ml/min) under vigorous stirring at 70°C to form a precipitate. The suspension was continuously stirred for 2 hours at 70°C, followed by cooling down to room temperature, filtering, and washing three times with deionized water. The filtered sample was dried at 110°C for 4 hours and calcined at 500°C in static air for 3 hours. Other x% ZnO-ZrO$_2$ catalysts were prepared following the same method. The supported ZnO/ZrO$_2$ catalyst was prepared by wet impregnation. ZrO$_2$ support was synthesized according to the coprecipitation method described above. ZrO$_2$ (1 g) was immersed in 25 ml of aqueous solution of Zn(NO$_3$)$_2$ with stoichiometric amount. The mixture was stirred at 110°C until the water had completely volatilized and then calcined at 500°C in air for 3 hours. The Cu/ZnO/Al$_2$O$_3$ catalyst was prepared by coprecipitation analogous to the procedure described by Behrens and Schlögl (6). Aqueous solution (100 ml) of metal nitrates [4.35 g of Cu(NO$_3$)$_2$·3H$_2$O, 2.68 g of Zn(NO$_3$)$_2$·6H$_2$O, and 1.12 g of Al(NO$_3$)$_3$·9H$_2$O] and aqueous solution (120 ml) of 3.82 g of Na$_2$CO$_3$ as a precipitant were added dropwise (at a flow rate of 3 ml/min) to a glass reactor with a starting volume of 200 ml of deionized water under vigorous stirring at 70°C. Controlling the pH of precipitation mother liquor to 7, and aging the precipitate for 2 hours after precipitation, followed by cooling down to room temperature, filtering, and washing seven times with deionized water. The filter cake was dried at 110°C for 4 hours and calcined at 350°C in static air for 3 hours. The commercial Cu/ZnO/Al$_2$O$_3$ catalyst (C307) was purchased from Nanjing Chemical Industrial Corporation of Sinopec for comparison. All catalysts were pressed, crushed, and sieved to the size of 40 to 80 mesh for the activity evaluation.

Catalyst evaluation

The activity tests of the catalysts for CO$_2$ hydrogenation to methanol were carried out in a tubular fixed-bed continuous-flow reactor equipped with gas chromatography (GC). Before the reaction, the catalyst (0.1 g, diluted with 0.4 g of quartz sand) was pretreated in a H$_2$ or N$_2$ stream (0.1 MPa and 20 ml/min) at given temperatures. The reaction was conducted under reaction conditions of 1.0 to 5.0 MPa, 180° to 400°C, V(H$_2$)/V(CO$_2$)/V(Ar) = 72:24:4, 64:32:4, or 77:19:5, and GHSV = 5000 to 33,000 ml/(g hour). The exit gas from the reactor was maintained at 150°C and immediately transported to the sample valve of the GC (Agilent 7890B), which was equipped with thermal conductivity (TCD) and flame ionization detectors (FIDs). Porapak N and 5A molecular sieve packed columns (2 m × 3.175 mm; Agilent) were connected to TCD, whereas TG-BOND Q capillary columns were connected to FID. The packed column was used for the analysis of CO$_2$, Ar, and CO, and the capillary column (30 m × 0.32 mm × 10 μm; Thermo Fisher) was used for hydrocarbons, alcohols, and other C-containing products. CO$_2$ conversion [denoted as X(CO$_2$)] and the carbon-based selectivity [denoted as S(product)] for the carbon-

containing products, including methane, methanol, and DME, were calculated using an internal normalization method. STY of methanol was denoted as STY(CH$_3$OH). All data were collected in 3 hours after the reaction started (unless otherwise specified).

X(CO$_2$), S(CH$_3$OH), S(CO), and STY(CH$_3$OH) were calculated as follows:

$$X(\text{CO}_2) =$$

$$\frac{f_{\text{CO}}A_{\text{CO}} + i(f_{\text{CH}_4}A_{\text{CH}_4} + f_{\text{CH}_3\text{OH}}A_{\text{CH}_3\text{OH}} + 2f_{\text{CH}_3\text{OCH}_3}A_{\text{CH}_3\text{OCH}_3})}{f_{\text{CO}_2}A_{\text{CO}_2} + f_{\text{CO}}A_{\text{CO}} + i(f_{\text{CH}_4}A_{\text{CH}_4} + f_{\text{CH}_3\text{OH}}A_{\text{CH}_3\text{OH}} + 2f_{\text{CH}_3\text{OCH}_3}A_{\text{CH}_3\text{OCH}_3})}$$

$$i = \frac{f_{\text{CH}_4\text{-TCD}}A_{\text{CH}_4\text{-TCD}}}{f_{\text{CH}_4\text{-FID}}A_{\text{CH}_4\text{-FID}}}$$

$$S(\text{CH}_3\text{OH}) =$$

$$\frac{f_{\text{CH}_3\text{OH}}A_{\text{CH}_3\text{OH}}}{f_{\text{CO}}A_{\text{CO}} + i(f_{\text{CH}_4}A_{\text{CH}_4} + f_{\text{CH}_3\text{OH}}A_{\text{CH}_3\text{OH}} + 2f_{\text{CH}_3\text{OCH}_3}A_{\text{CH}_3\text{OCH}_3})}$$

$$S(\text{CO}) =$$

$$\frac{f_{\text{CO}}A_{\text{CO}}}{f_{\text{CO}}A_{\text{CO}} + i(f_{\text{CH}_4}A_{\text{CH}_4} + f_{\text{CH}_3\text{OH}}A_{\text{CH}_3\text{OH}} + 2f_{\text{CH}_3\text{OCH}_3}A_{\text{CH}_3\text{OCH}_3})}$$

$$\text{STY}(\text{CH}_3\text{OH}) = \frac{\text{GHSV}}{\text{SA} \times 22.4} \times V\%(\text{CO}_2) \times X(\text{CO}_2) \times S(\text{CO}_2)$$
$$\times M_{\text{CH}_3\text{OH}}$$

Catalyst characterization

The XRD results were collected on a Philips PW1050/81 diffractometer operating in Bragg-Brentano focusing geometry and using Cu Kα radiation (λ = 1.5418 Å) from a generator operating at 40 kV and 30 mA. TEM images were obtained with a JEM-2100 microscope at 200 kV. The samples were prepared by placing a drop of nanoparticle ethanol suspension onto a lacey support film and by allowing the solvent to evaporate. Element mappings were obtained with a JEM-ARM200F microscope. UV-vis spectrum was obtained with a PerkinElmer 25 UV-vis spectrometer in the wavelength range of 350 to 800 nm, with a resolution of 1 nm. The UV laser source (244 and 266 nm) was a Coherent Innova 300 C FreD continuous wave UV laser equipped with an intracavity frequency-doubling system using a BBO crystal to produce second harmonic generation outputs at different wavelengths. The UV laser source (325 nm) was a Coherent DPSS 325 Model 200 325-nm single-frequency laser. UV Raman spectra were recorded on a home-assembled UV Raman spectrograph using a Jobin-Yvon T64000 triple-stage spectragraph with a spectral resolution of 2 cm^{-1} coupled with a UV-sensitive charge-coupled device detector. XPS was performed using a Thermo Fisher ESCALAB 250Xi with Al K radiation (15 kV, 10.8 mA, hv = 1486.6 eV) under ultrahigh vacuum (5 × 10^{-7} Pa), calibrated internally by the carbon deposit C(1s) (E_b = 284.6 eV). The CO$_2$/H$_2$-TPD of the catalysts was conducted with an adsorption/desorption system. A 100-mg sample was treated in situ in a H$_2$ or He stream (30 ml/min) at 300°C for 1 hour, flushed by a He stream (30 ml/min) at 300°C for 30 min to clean its surface, and then cooled to 50°C. It was then returned to the CO$_2$/H$_2$ stream for 60 min, and afterward, the sample was flushed by the He stream until a stable baseline was obtained. TPD measurements were then conducted from 50° to 600°C.

The temperature increase rate was 10°C/min. The changes of CO_2/H_2 were monitored by AutoChem 2910 with a TCD detector. The system was coupled to an OmniStar 300 mass spectrometer to detect other products in the gas phase. The TPR of the catalysts was conducted with the same system used in TPD. The samples were treated with He at 130°C for 1 hour, and then 5% H_2/Ar was used as carrier gas of TCD to conduct the TPR with 10°C/min from 50° to 800°C. H_2-D_2 exchange experiments were performed in a flow reactor at 280°C. The formation rate of HD was measured by mass signal intensity (ion current). The 0.1-g sample was reduced with H_2 (10 ml/min) at 280°C for 1 hour. Then, D_2 (10 ml/min) was mixed with H_2 and together passed the catalyst sample. Reaction products HD, H_2, and D_2 were analyzed with a mass spectrometer (GAM200, InProcess Instruments). The mass/charge ratio (m/z) values used are 2 for H_2, 4 for D_2, and 3 for HD. In situ DRIFTS investigations were performed using a Fourier transform infrared (FTIR) spectrometer (Thermo Fisher, Nicolet 6700) equipped with a mercury cadmium telluride detector. Before measurement, each catalyst was treated with H_2 at 300°C for 2 hours and then purged with N_2 at 450°C for 2 hours. The catalyst was subsequently cooled down to 280°C. The background spectrum was obtained at 280°C in N_2 flow. Then, the sample was exposed to a CO_2/H_2 mixture (10 ml/min CO_2 and 30 ml/min H_2) for 90 min. The in situ DRIFT spectra were recorded by collecting 64 scans at a resolution of 4 cm^{-1}. IR-MS experiments were performed by combining DRIFTS and MS. The products detected by MS were warmed to be the gas phase. The specific surface area was determined by N_2 adsorption using a Micromeritics ASAP 2020 system.

DFT calculation

Spin-polarized DFT calculations were performed with the VASP 5.3.5 package (45). The generalized gradient approximation based on Perdew-Burke-Ernzerhof exchange-correlation functional and projected augmented wave method accounting for valence-core interactions were used throughout (46). The kinetic energy cutoff of the plane-wave basis set was set to 400 eV. A Gaussian smearing of the population of partial occupancies with a width of 0.1 eV was used during iterative diagonalization of the Kohn-Sham Hamiltonian. The threshold for energy convergence in each iteration was set to 10^{-5} eV. Convergence was assumed when forces on each atom were less than 0.05 eV/Å in the geometry optimization. The minimum-energy reaction pathways and the corresponding transition states were determined using the nudged elastic band method with improved tangent estimate (CI-NEB) implemented in VASP (47). The maximum energy geometry along the reaction path obtained with the NEB method was further optimized using a quasi-Newton algorithm. In this step, only the adsorbates and the active center of the metal site were relaxed. Frequency analysis of the stationary points was performed by means of the finite difference method as implemented in VASP 5.3.5. Small displacements (0.02 Å) were used to estimate the numerical Hessian matrix. The transition states were confirmed by the presence of a single imaginary frequency corresponding to the specific reaction path.

Both the unit lattice vectors and atoms of hexagonal wurtzite structure ZnO were fully optimized in the first step. The optimized lattice parameters for bulk ZnO are $a = b = 3.289$ Å and $c = 5.312$ Å, which are coherent with the experimental values of $a = b = 3.249$ Å and $c = 5.206$ Å (48). The Zn-terminated (0001) polar surface slab model of ZnO was constructed by a periodic $4 \times 4 \times 1$ supercell with five Zn-O sublayers and separated by a vacuum layer of 15 Å along the surface normal direction to avoid spurious interactions between the periodic slab models. The top two Zn-O sublayers were fully relaxed, whereas

the lowest three layers were fixed at the optimized atomic bulk positions during all the surface calculations. Monkhorst-Pack mesh of $8 \times 8 \times 6$ k-points was used to sample the Brillouin zone for the bulk ZnO, and it was restricted to $2 \times 2 \times 1$ k-points for the supercell surface slab model due to the computational time demands. To eliminate the artificial dipole moment within the slab model of polar ZnO surface, all the oxygen atoms at the bottom of the slab model were saturated by adding pseudo-hydrogen atoms, each containing a positive charge of +0.5 $|e|$. This strategy effectively removes the internal polarization within the slab, as indicated by the flatter projection of the Hartree potential along the direction of the surface normal compared to other dipole correction methods.

The optimized lattice parameters for tetragonal ZrO_2 bulk are $a = b = 3.684$ Å and $c = 5.222$ Å, which are in line with the experimental values of $a = b = 3.612$ Å and $c = 5.212$ Å (49). The most stable (101) surface of the ZrO_2 tetragonal phase was simulated by a $2 \times 3 \times 1$ supercell slab model, including three ZrO_2 sublayers (each includes two oxygen atomic layers and one Zr atomic layer), separated by a vacuum layer with a thickness of 15 Å along the surface normal direction to avoid spurious interactions between the periodic slab models. To take into account the effect of Zn^{2+} doping, one of the Zr^{4+}-O^{2-} moiety on the surface was replaced by a Zn^{2+} cation and an oxygen vacancy (Zn^{2+}-O_v). The atoms of the top ZrO_2 layer were fully optimized, whereas the other two ZrO_2 layers at the bottom were fixed at their optimized bulk positions throughout the surface calculations. The on-site Coulomb correction for the Zr 4d states of the ZrO_2 bulk and Zn-ZrO_2 surface was included by DFT + U approach with a U_{eff} value of 4.0 eV. K-point grids of $8 \times 8 \times 6$ and $2 \times 2 \times 1$ generated by Monkhorst-Pack scheme were used to sample the Brillouin zones of the ZrO_2 bulk and Zn-ZrO_2 supercell surface slab model, respectively.

The adsorption energy of the reaction intermediate was calculated as $\Delta E_{\text{ads}} = E_{\text{adsorbate+surface}} - E_{\text{adsorbate}} - E_{\text{clean-surface}}$. The activation energy (ΔE_a) of a chemical reaction was defined as the energy difference between the initial and transition states, whereas the reaction energy (ΔE) was defined as the energy difference between the initial and final states. The enthalpy, entropy, and Gibbs free energy of each species were calculated by vibrational frequency analysis based on harmonic normal mode approximation using the finite difference method in VASP. The threshold for energy convergence for each iteration was set to 10^{-8} eV, and the forces on each atom were 0.01 eV/Å. The Gibbs free energy for a given species is $G(T, P) = E_e + E_{\text{trans}} + E_{\text{rot}} + E_{\text{vib}} + PV - T(S_{\text{trans}} + S_{\text{rot}} + S_{\text{vib}})$:

where

$$E_{\text{trans}} = \frac{3}{2}RT$$

$$E_{\text{rot}} = RT \text{ (for linear molecule)}$$

$$E_{\text{rot}} = \frac{3}{2}RT \text{ (for non-linear molecule)}$$

$$E_{\text{vib}} = R\sum_n \frac{h\nu_n}{k_B}\left(\frac{1}{2} + \frac{1}{e^{h\nu_n/k_B T} - 1}\right)$$

$$S_{\text{trans}} = R\left(\ln q_{\text{trans}} + \frac{5}{2}\right), \text{ where } q_{\text{trans}} = \left(\frac{2\pi m k_B T}{h^2}\right)^{3/2}\frac{k_B T}{P}$$

$$S_{\text{rot}} = R\left(\ln q_{\text{rot}} + 1\right) \text{ (for linear molecule)},$$

$$\text{where } q_{\text{rot}} = \frac{1}{\sigma}\left(\frac{8\pi^2 k_B T}{h^2}\right) \times I$$

$$S_{\text{rot}} = R\left(\ln q_{\text{rot}} + \frac{3}{2}\right) \text{ (for nonlinear molecule)},$$

$$\text{where } q_{\text{rot}} = \frac{\sqrt{\pi}}{\sigma}\left(\frac{8\pi^2 k_B T}{h^2}\right)^{3/2} \times \sqrt{I_x \times I_y \times I_z}$$

$$S_{\text{vib}} = R\sum_n\left(\frac{h\nu_n/k_B T}{e^{h\nu_n/k_B T} - 1} - \ln(1 - e^{-h\nu_n/k_B T})\right)$$

where I is the moment of inertia, σ is the rotational symmetry number, and m is the mass of the molecule. The translational, rotational, and vibrational enthalpic and entropic contributions of gas-phase molecules were calculated by considering them as ideal gases. For adsorbed molecules and transition states on the surface, the rotational and translational contributions were converted into vibration modes. We also approximated that the PV term of the surface species is negligible because it is very small with regard to the energetic terms, and thus, we considered $G(T, P) = E_e + E_{\text{vib}} - T \times S_{\text{vib}}$ in this case.

SUPPLEMENTARY MATERIALS

Supplementary material for this article is available at http://advances.sciencemag.org/cgi/content/full/3/10/e1701290/DC1

table S1. The BET results of catalysts and intrinsic property.
table S2. The catalytic performance of mechanically mixed and supported catalysts.
table S3. DRIFT peak assignments of the surface species for the $CO_2 + H_2(D_2)$ reaction on 13% ZnO-ZrO_2.
fig. S1. The dependence of methanol selectivity on the $Zn/(Zn + Zr)$ molar ratio at a 10% CO_2 conversion.
fig. S2. The effect of pressure, H_2/CO_2 ratio, and GHSV on CO_2 hydrogenation.
fig. S3. XRD patterns of ZnO-ZrO_2 catalysts.
fig. S4. HRTEM of the 13% ZnO-ZrO_2 catalyst.
fig. S5. The UV-vis absorbance and Raman spectra of ZnO-ZrO_2.
fig. S6. XPS of ZnO, ZrO_2, and 13% ZnO-ZrO_2.
fig. S7. H_2-TPR of ZnO, ZrO_2, and 13% ZnO-ZrO_2.
fig. S8. XRD of mechanically mixed and supported catalysts.
fig. S9. DRIFT results of $CO_2 + H_2$ substituted by $CO_2 + D_2$.
fig. S10. Structure of ZrO_2 and ZnO-ZrO_2.
fig. S11. Local geometries of the reaction intermediates of CO_2 hydrogenation to methanol via formate on the ZnO-ZrO_2 (101) surface.
fig. S12. Local geometries of the reaction intermediates of CO_2 hydrogenation to methanol via CO on the ZnO-ZrO_2 (101) surface.
fig. S13. Structure of ZnO.
fig. S14. Hartree potential of the Zn-terminated ZnO (0001) surface calculated by different dipole correction methods.
fig. S15. Local geometries of the reaction intermediates on the ZnO (0001) surface.
fig. S16. Reaction diagram of CO_2 hydrogenation to CH_3OH via formate on the Zn-terminated ZnO (0001) surface.
fig. S17. The catalytic performance contrast of the ZnO-ZrO_2 catalyst for $CO_2 + H_2$ and $CO + H_2$.
fig. S18. The catalytic performance contrast of $Cu/ZnO/Al_2O_3$ and ZnO-ZrO_2 catalysts for CO_2 hydrogenation.
fig. S19. The stability test of the $Cu/ZnO/Al_2O_3$ catalyst.

REFERENCES AND NOTES

1. G. A. Olah, A. Goeppert, G. K. Surya Prakash, *Beyond Oil and Gas: The Methanol Economy* (Wiley-VCH, 2011).
2. A. Goeppert, M. Czaun, J.-P. Jones, G. K. Surya Prakash, G. A. Olah, Recycling of carbon dioxide to methanol and derived products—Closing the loop. *Chem. Soc. Rev.* **43**, 7995–8048 (2014).
3. M. D. Porosoff, B. Yan, J. G. Chen, Catalytic reduction of CO_2 by H_2 for synthesis of CO, methanol and hydrocarbons: Challenges and opportunities. *Energy Environ. Sci.* **9**, 62–73 (2016).
4. G. Centi, S. Perathoner, Opportunities and prospects in the chemical recycling of carbon dioxide to fuels. *Catal. Today* **148**, 191–205 (2009).
5. E. V. Kondratenko, G. Mul, J. Baltrusaitis, G. O. Larrazábal, J. Pérez-Ramírez, Status and perspectives of CO_2 conversion into fuels and chemicals by catalytic, photocatalytic and electrocatalytic processes. *Energy Environ. Sci.* **6**, 3112–3135 (2013).
6. M. Behrens, R. Schlögl, How to prepare a good Cu/ZnO catalyst or the role of solid state chemistry for the synthesis of nanostructured catalysts. *Z. Anorg. Allg. Chem.* **639**, 2683–2695 (2013).
7. M. Behrens, F. Studt, I. Kasatkin, S. Kühl, M. Hävecker, F. Abild-Pedersen, S. Zander, F. Girgsdies, P. Kurr, B.-L. Kniep, M. Tovar, R. W. Fischer, J. K. Nørskov, R. Schlögl, The active site of methanol synthesis over Cu/ZnO/Al₂O₃ industrial catalysts. *Science* **336**, 893–897 (2012).
8. H. Zhan, F. Li, C. Xin, N. Zhao, F. Xiao, W. Wei, Y. Sun, Performance of the La–Mn–Zn–Cu–O based perovskite precursors for methanol synthesis from CO_2 hydrogenation. *Catal. Lett.* **145**, 1177–1185 (2015).
9. S. Kuld, M. Thorhauge, H. Falsig, C. F. Elkjær, S. Helveg, I. Chorkendorff, J. Sehested, Quantifying the promotion of Cu catalysts by ZnO for methanol synthesis. *Science* **352**, 969–974 (2016).
10. S. Kattel, P. J. Ramirez, J. G. Chen, J. A. Rodriguez, P. Liu, Active sites for CO_2 hydrogenation to methanol on Cu/ZnO catalysts. *Science* **355**, 1296–1299 (2017).
11. Y. Amenomiya, Methanol synthesis from $CO_2 + H_2$ II. Copper-based binary and ternary catalysts. *Appl. Catal.* **30**, 57–68 (1987).
12. K. Larmier, W.-C. Liao, S. Tada, E. Lam, R. Verel, A. Bansode, A. Urakawa, A. Comas-Vives, C. Copéret, CO_2-to-methanol hydrogenation on zirconia-supported copper nanoparticles: Reaction intermediates and the role of the metal–support interface. *Angew. Chem. Int. Ed.* **129**, 2358–2363 (2017).
13. S. Kattel, B. Yan, Y. Yang, J. G. Chen, P. Liu, Optimizing binding energies of key intermediates for CO_2 hydrogenation to methanol over oxide-supported copper. *J. Am. Chem. Soc.* **138**, 12440–12450 (2016).
14. X.-L. Liang, X. Dong, G.-D. Lin, H.-B. Zhang, Carbon nanotube-supported Pd–ZnO catalyst for hydrogenation of CO_2 to methanol. *Appl. Catal. B* **88**, 315–322 (2009).
15. H. Bahruji, M. Bowker, G. Hutchings, N. Dimitratos, P. Wells, E. Gibson, W. Jones, C. Brookes, D. Morgan, G. Lalev, Pd/ZnO catalysts for direct CO_2 hydrogenation to methanol. *J. Catal.* **343**, 133–146 (2016).
16. J. Wu, M. Saito, M. Takeuchi, T. Watanabe, The stability of Cu/ZnO-based catalysts in methanol synthesis from a CO_2-rich feed and from a CO-rich feed. *Appl. Catal. A. Gen.* **218**, 235–240 (2001).
17. S. A. Kondrat, P. J. Smith, P. P. Wells, P. A. Chater, J. H. Carter, D. J. Morgan, E. M. Fiordaliso, J. B. Wagner, T. E. Davies, L. Lu, J. K. Bartley, S. H. Taylor, M. S. Spencer, C. J. Kiely, G. J. Kelly, C. W. Park, M. J. Rosseinsky, G. J. Hutchings, Stable amorphous georgeite as a precursor to a high-activity catalyst. *Nature* **531**, 83–87 (2016).
18. J. Graciani, K. Mudiyanselage, F. Xu, A. E. Baber, J. Evans, S. D. Senanayake, D. J. Stacchiola, P. Liu, J. Hrbek, J. F. Sanz, J. A. Rodriguez, Highly active copper-ceria and copper-ceria-titania catalysts for methanol synthesis from CO_2. *Science* **345**, 546–550 (2014).
19. X. Yang, X. Yang, S. Kattel, S. D. Senanayake, J. A. Boscoboinik, X. Nie, J. Graciani, J. A. Rodriguez, P. Liu, D. J. Stacchiola, J. G. Chen, Low pressure CO_2 hydrogenation to methanol over gold nanoparticles activated on a CeO_x/TiO_2 interface. *J. Am. Chem. Soc.* **137**, 10104–10107 (2015).
20. F. Studt, I. Sharafutdinov, F. Abild-Pedersen, C. F. Elkjær, J. S. Hummelshøj, S. Dahl, I. Chorkendorff, J. K. Nørskov, Discovery of a Ni-Ga catalyst for carbon dioxide reduction to methanol. *Nat. Chem.* **6**, 320–324 (2014).
21. I. Sharafutdinov, C. F. Elkjær, H. W. P. de Carvalho, D. Gardini, G. L. Chiarello, C. D. Damsgaard, J. B. Wagner, J.-D. Grunwaldt, S. Dahl, I. Chorkendorff, Intermetallic compounds of Ni and Ga as catalysts for the synthesis of methanol. *J. Catal.* **320**, 77–88 (2014).
22. E. M. Fiordaliso, I. Sharafutdinov, H. W. P. Carvalho, J.-D. Grunwaldt, T. W. Hansen, I. Chorkendorff, J. B. Wagner, C. D. Damsgaard, Intermetallic GaPd₂ nanoparticles on SiO₂ for low-pressure CO_2 hydrogenation to methanol: Catalytic performance and in situ characterization. *ACS Catal.* **5**, 5827–5836 (2015).
23. J. Ye, C. Liu, D. Mei, Q. Ge, Active oxygen vacancy site for methanol synthesis from CO_2 hydrogenation on In_2O_3(110): A DFT study. *ACS Catal.* **3**, 1296–1306 (2013).
24. K. Sun, Z. Fan, J. Ye, J. Yan, Q. Ge, Y. Li, W. He, W. Yang, C.-j. Liu, Hydrogenation of CO_2 to methanol over In_2O_3 catalyst. *J. CO_2 Util.* **12**, 1–6 (2015).
25. O. Martin, A. J. Martín, C. Mondelli, S. Mitchell, T. F. Segawa, R. Hauert, C. Drouilly, D. Curulla-Ferré, J. Pérez-Ramírez, Indium oxide as a superior catalyst for methanol synthesis by CO_2 hydrogenation. *Angew. Chem. Int. Ed.* **55**, 6261–6265 (2016).
26. R. D. Shannon, Revised effective ionic radii and systematic studies of interatomic distances in halides and chalcogenides. *Acta Crystallogr. A* **32**, 751–767 (1976).
27. A. Cimino, F. S. Stone, Oxide solid solutions as catalysts. *Adv. Catal.* **47**, 141–306 (2002).
28. H. Kim, K. M. Kosuda, R. P. Van Duyne, P. C. Stair, Resonance Raman and surface- and tip-enhanced Raman spectroscopy methods to study solid catalysts and heterogeneous catalytic reactions. *Chem. Soc. Rev.* **39**, 4820–4844 (2010).
29. F. Fan, Q. Xu, H. Xia, K. Sun, Z. Feng, C. Li, UV Raman spectroscopic characterization of catalytic materials. *Chin. J. Catal.* **30**, 717–739 (2009).
30. M. Li, Z. Feng, P. Ying, Q. Xin, C. Li, Phase transformation in the surface region of zirconia and doped zirconia detected by UV Raman spectroscopy. *Phys. Chem. Chem. Phys.* **5**, 5326–5332 (2003).

31. L. Shi, K.-C. Tin, N.-B. Wong, Thermal stability of zirconia membranes. *J. Mater. Sci.* **34**, 3367–3374 (1999).

32. T. Shido, Y. Iwasawa, The effect of coadsorbates in reverse water-gas shift reaction on ZnO, in relation to reactant-promoted reaction mechanism. *J. Catal.* **140**, 575–584 (1993).

33. J. Tabatabaei, B. H. Sakakini, K. C. Waugh, On the mechanism of methanol synthesis and the water-gas shift reaction on ZnO. *Catal. Lett.* **110**, 77–84 (2006).

34. I. A. Fisher, A. T. Bell, In-situ infrared study of methanol synthesis from H_2/CO_2 over Cu/SiO_2 and $Cu/ZrO_2/SiO_2$. *J. Catal.* **172**, 222–237 (1997).

35. K. Pokrovski, K. T. Jung, A. T. Bell, Investigation of CO and CO_2 adsorption on tetragonal and monoclinic zirconia. *Langmuir* **17**, 4297–4303 (2001).

36. C. Schild, A. Wokaun, A. Baiker, On the mechanism of CO and CO_2 hydrogenation reactions on zirconia-supported catalysts: A diffuse reflectance FTIR study: Part II. Surface species on copper/zirconia catalysts: Implications for methanol synthesis selectivity. *J. Mol. Catal.* **63**, 243–254 (1990).

37. A. Goguet, F. C. Meunier, D. Tibiletti, J. P. Breen, R. Burch, Spectrokinetic investigation of reverse water-gas-shift reaction intermediates over a Pt/CeO_2 catalyst. *J. Phys. Chem. B* **108**, 20240–20246 (2004).

38. X. Wang, H. Shi, J. H. Kwak, J. Szanyi, Mechanism of CO_2 hydrogenation on Pd/Al_2O_3 catalysts: Kinetics and transient DRIFTS-MS studies. *ACS Catal.* **5**, 6337–6349 (2015).

39. L. C. Grabow, M. Mavrikakis, Mechanism of methanol synthesis on Cu through CO_2 and CO hydrogenation. *ACS Catal.* **1**, 365–384 (2011).

40. L. Martínez-Suárez, N. Siemer, J. Frenzel, D. Marx, Reaction network of methanol synthesis over Cu/ZnO nanocatalysts. *ACS Catal.* **5**, 4201–4218 (2015).

41. S. A. French, A. A. Sokol, S. T. Bromley, R. A. Catlow, S. C. Rogers, F. King, P. Sherwood, From CO_2 to methanol by hybrid QM/MM embedding. *Angew. Chem. Int. Ed.* **113**, 4569–4572 (2001).

42. Y.-F. Zhao, R. Rousseau, J. Li, D. Mei, Theoretical study of syngas hydrogenation to methanol on the polar Zn-terminated ZnO(0001) surface. *J. Phys. Chem. C* **116**, 15952–15961 (2012).

43. R. Gaikwad, A. Bansode, A. Urakawa, High-pressure advantages in stoichiometric hydrogenation of carbon dioxide to methanol. *J. Catal.* **343**, 127–132 (2017).

44. X. An, J. Li, Y. Zuo, Q. Zhang, D. Wang, J. Wang, A Cu/Zn/Al/Zr fibrous catalyst that is an improved CO_2 hydrogenation to methanol catalyst. *Catal. Lett.* **118**, 264–269 (2007).

45. G. Kresse, J. Furthmüller, Efficient iterative schemes for ab initio total-energy calculations using a plane-wave basis set. *Phys. Rev. B* **54**, 11169–11186 (1996).

46. J. P. Perdew, K. Burke, Y. Wang, Generalized gradient approximation for the exchange-correlation hole of a many-electron system. *Phys. Rev. B Condens. Matter* **54**, 16533–16539 (1996).

47. G. Henkelman, H. Jónsson, Improved tangent estimate in the nudged elastic band method for finding minimum energy paths and saddle points. *J. Chem. Phys.* **113**, 9978–9985 (2000).

48. M. Schreyer, L. Guo, S. Thirunahari, F. Gao, M. Garland, Simultaneous determination of several crystal structures from powder mixtures: The combination of powder X-ray diffraction, band-target entropy minimization and Rietveld methods. *J. Appl. Cryst.* **47**, 659–667 (2014).

49. N. Igawa, Y. Ishii, Crystal structure of metastable tetragonal zirconia up to 1473 K. *J. Am. Ceram. Soc.* **84**, 1169–1171 (2001).

Citation: J. Wang, G. Li, Z. Li, C. Tang, Z. Feng, H. An, H. Liu, T. Liu, C. Li, A highly selective and stable ZnO-ZrO₂ solid solution catalyst for CO₂ hydrogenation to methanol. *Sci. Adv.* **3**, e1701290 (2017).

Science Advances

A highly selective and stable ZnO-ZrO$_2$ solid solution catalyst for CO$_2$ hydrogenation to methanol

Jijie Wang, Guanna Li, Zelong Li, Chizhou Tang, Zhaochi Feng, Hongyu An, Hailong Liu, Taifeng Liu and Can Li

ARTICLE TOOLS	http://advances.sciencemag.org/content/3/10/e1701290
SUPPLEMENTARY MATERIALS	http://advances.sciencemag.org/content/suppl/2017/10/02/3.10.e1701290.DC1
REFERENCES	This article cites 48 articles, 4 of which you can access for free http://advances.sciencemag.org/content/3/10/e1701290#BIBL
PERMISSIONS	http://www.sciencemag.org/help/reprints-and-permissions

Use of this article is subject to the Terms of Service